




Cite this: *J. Mater. Chem. A*, 2019, 7, 15722

(C₆H₅NH₃)BiI₄: a lead-free perovskite with >330 days humidity stability for optoelectronic applications†

Xiao-Lei Li,  Li-Li Gao, Bin Ding,  Qian-Qian Chu, Zhen Li and Guan-Jun Yang *

A key challenge in the eco-friendly optoelectronic materials field is to find highly stable and nontoxic perovskite materials. Here, we report the optoelectronic properties and stability of the (C₆H₅NH₃)BiI₄ perovskite material. Using an eco-friendly gas pump treatment technique, a dense and pinhole-free (C₆H₅NH₃)BiI₄ film was fabricated. Remarkably, a large-area (>20 cm²) Bi-based perovskite film was obtained, which is the largest Bi-based perovskite film ever reported. Besides, the (C₆H₅NH₃)BiI₄ perovskite exhibits good solubility in ethanol, which is a safe and eco-friendly solvent. Thermogravimetric analysis results show the beginning of weight loss at ~184 °C, suggesting excellent heat stability of this material. Most importantly, the (C₆H₅NH₃)BiI₄ material can tolerate continuous moisture exposure for 334 days in ambient air owing to the presence of a hydrophobic organic chain. To the best of our knowledge, this is the longest moisture stability reported for lead-free perovskite materials so far. This work paves the way for realizing highly stable and nontoxic perovskite materials for potential optoelectronic applications.

Received 5th March 2019

Accepted 10th May 2019

DOI: 10.1039/c9ta02421b

rsc.li/materials-a

Introduction

Organic-inorganic lead-based perovskite materials are emerging as highly fascinating semiconductors for use in a variety of applications, including photovoltaic devices,^{1–3} light-emitting diodes (LED),^{4,5} radiation detectors,⁶ nanocrystal scintillators,⁷ and semiconducting ferroelectrics.⁸ To date, the power conversion efficiency (PCE) of single-junction perovskite solar cells (PVSCs) has been certified to be well above 23%.⁹ Recently, lead-based perovskite LEDs with an external quantum efficiency of over 20% has been reported.^{4,5} However, almost all top-performing optoelectronic devices were made of lead-based perovskite materials with unsatisfactory stability. Human exposure to lead is pernicious to the nervous and reproductive systems, and this may weaken the market acceptance of this emerging technology.^{10,11} In addition, the use of toxic solvents (*N,N*-dimethylformamide, dimethyl sulfoxide, and chlorobenzene) in the preparation of perovskites is another issue that needs to be solved as well, since these solvents can easily penetrate into the human body and diffuse into the atmosphere to cause global environmental pollution.¹² Therefore, it is highly desirable to search for highly stable and nontoxic perovskite optoelectronic

materials that can be prepared using eco-friendly solvents and solution-based deposition methods.

Previously, extensive efforts were devoted for the development of eco-friendly halide perovskite optoelectronic materials both experimentally and theoretically.^{13–16} The elements used to replace lead mainly include Sn,^{17–20} Ge,^{21,22} Bi,^{23–30} Sb,³¹ and Cu.^{32–34} Among these, Bi-based materials have attracted considerable attention as candidates for lead-free perovskites due to their long-term stability.²³ Moreover, Bi³⁺ with 6s² lone pairs¹⁵ might result in excellent optoelectronic properties. MA₃Bi₂I₉ and Cs₃Bi₂I₉ are the most extensively studied Bi-based perovskite materials. In 2015, Johansson *et al.* reported the photovoltaic performance of Bi-based halide compounds (Cs₃Bi₂I₉ and MA₃Bi₂I₉).²³ However, the film quality of Cs₃Bi₂I₉ and MA₃Bi₂I₉ was not satisfactory.²³ In 2017, Zhang *et al.* fabricated a highly compact, pinhole-free, and large-grained MA₃Bi₂I₉ film by a costly vacuum deposition method.²⁴ In 2018, Park *et al.* reported the resistive switching properties of A₃Bi₂I₉ (A is either Cs⁺ or Rb⁺) and the devices showed a low operating voltage, large on/off ratio, relatively high endurance, and high retention.²⁹ Besides, Tang *et al.* reported a new photoluminescence quantum yield record (54.1%) for blue emission, Bi-based perovskite quantum dots.³⁰

Bi-based materials usually exhibit a much better intrinsic stability than MAPbI₃. For example, MA₃Bi₂I₉ and Cs₃Bi₂I₉ exhibit >25 days stability in air while MAPbI₃ becomes yellow after 5 days.^{23,25} However, compared to silicon-based solar cells with 20 years stability, how to realize lead-free perovskites with a higher excellent intrinsic stability is still a big challenge in this

State Key Laboratory for Mechanical Behavior of Materials, School of Materials Science and Engineering, Xi'an Jiaotong University, Xi'an 710049, P. R. China. E-mail: ygj@mail.xjtu.edu.cn

† Electronic supplementary information (ESI) available. See DOI: 10.1039/c9ta02421b

field. One effective method to improve the stability of lead-based perovskites is to replace hygroscopic cations (MA^+ or FA^+) with hydrophobic groups, such as phenylethylammonium (PEA)³⁵ and butylammonium (BA).³⁶ For example, Tsai *et al.* reported $(\text{BA})_2(\text{MA})_3\text{Pb}_4\text{I}_{13}$ -based solar cells with a high PCE of 12.52% and outstanding moisture stability.³⁶ Recently, $(\text{PMA})_2\text{CuBr}_4$ -based perovskites with high stability toward humidity, heat, and ultraviolet light have been achieved.³⁴ However, realizing superior stability toward humidity and heat in organic–inorganic hybrid Bi-based perovskites is still a major challenge. This prompted us to explore highly stable Bi-based perovskite materials for potential optoelectronic applications.

In this paper, we report the optoelectronic properties and stability of PHABiI_4 ($\text{PHA} = \text{C}_6\text{H}_5\text{NH}_3^+$) materials. This work is inspired by the research on low-dimensional perovskites with enhanced stability.^{34–36} Therefore, it is rational that Bi-based materials with hydrophobic PHA cations should well overcome the problems of toxicity and poor stability of lead-based perovskites in the meantime. The reason why we use PHA also includes the smaller molecular radius of PHA than PEA or PMA. Xiao *et al.*¹⁵ reported that the band gap can be lowered by controlling factors such as the molecular radius of the spacing cation. So, we speculate that PHABiI_4 may have a wider absorption range than PEABiI_4 or PMABiI_4 . We successfully fabricated a dense and pinhole-free PHABiI_4 film *via* an

eco-friendly gas pump treatment technique. Remarkably, we obtained a large-area ($>20 \text{ cm}^2$) Bi-based perovskite film, which is the largest Bi-based perovskite film ever reported. Besides, the PHABiI_4 material exhibits excellent moisture stability of more than 330 days in ambient air at 50–70% relative humidity (RH). To the best of our knowledge, this is the longest moisture stability reported for lead-free perovskite materials so far. Moreover, the PHABiI_4 material exhibits good solubility in ethanol, which is an eco-friendly solvent for solution processing other than water.

Results and discussion

The crystal structure of PHABiI_4 is similar to that of $\text{C}_6\text{H}_5\text{NBiI}_4$ perovskites (see Fig. 1a).²⁷ It consists of one-dimensional edge-sharing chains composed of BiI_6 octahedra connected by a hydrogen bonding interaction.²⁷ The X-ray diffraction (XRD) patterns of PHABiI_4 in comparison to those of BiI_3 and $\text{C}_6\text{H}_5\text{NH}_3\text{I}$ are also given in Fig. 1b. The dominant diffraction peaks of the PHABiI_4 perovskite are at $2\theta = 9.07^\circ$, 25.45° , and 26.58° . In addition, the experimental XRD results show good consistency with XRD simulation results (see Fig. S1†). We note that no additional peaks related to possible residues of BiI_3 (three dominant peaks at $2\theta = 10.23^\circ$, 20.48° , and 21.48°) have been observed in the XRD pattern of PHABiI_4 . However, one

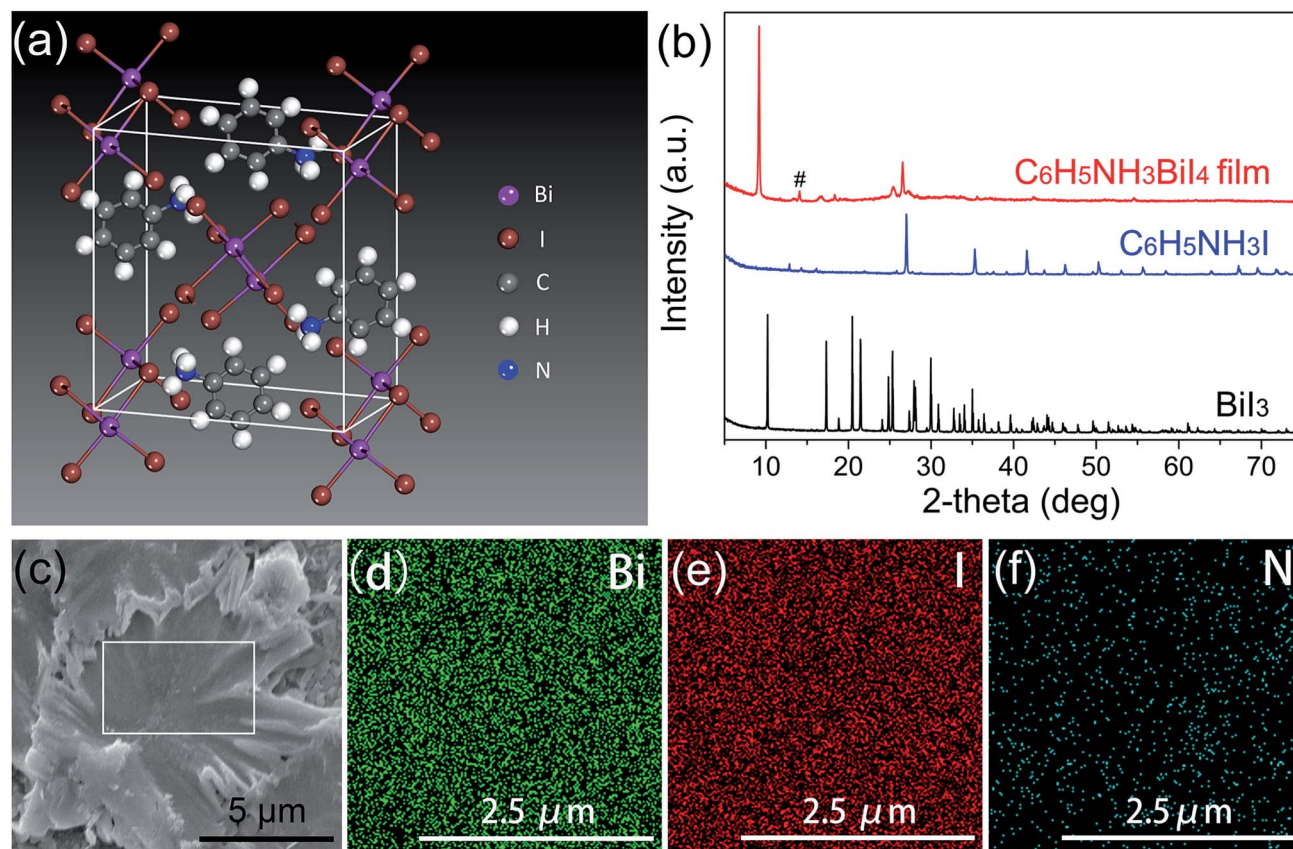


Fig. 1 (a) Schematic picture of the $(\text{C}_6\text{H}_5\text{NH}_3)\text{BiI}_4$ structure. (b) XRD patterns of $(\text{C}_6\text{H}_5\text{NH}_3)\text{BiI}_4$, BiI_3 , and $\text{C}_6\text{H}_5\text{NH}_3\text{I}$ compounds. # indicates the peak of the $\text{C}_6\text{H}_5\text{NH}_3\text{I}$ compound. (c) Scanning electron microscopy (SEM) image of the $(\text{C}_6\text{H}_5\text{NH}_3)\text{BiI}_4$ film prepared by heat treatment. (d–f) Elemental mapping of Bi, I, and N in the area indicated by the white box.

peak ($2\theta = 14.10^\circ$) was observed in the XRD pattern of PHABiI₄, which can be attributed to traces of the C₆H₅NH₃I compound (see Fig. 1b and S1†). The energy-dispersive X-ray spectrum (EDX) is shown in Fig. 1c–e, wherein the distribution of Bi, I, and N elements in the PHABiI₄ film is homogeneous. The obtained Bi/I atomic ratio is approximately 1 : 4, which is consistent with the stoichiometry in the molecule's formula (Fig. S2†).

The morphology of the perovskite film is a key factor that could severely limit device performance. To date, it is challenging to fabricate dense and pinhole-free Bi-based perovskite films by solution-based deposition methods.^{23,37} Consequently, it is vital to develop robust methods for fabricating high-quality Bi-based perovskite films. Here, we successfully fabricated dense and pinhole-free Bi-based perovskite films *via* a green gas pump treatment technique. For comparison, the schematic mechanism, photographs and SEM images of the PHABiI₄ films fabricated by the conventional heat treatment and gas pump treatment in ambient air at 30% RH are shown in Fig. 2. The PHABiI₄ film prepared by heat treatment (DMF as the solvent) shows a coarse surface morphology with very poor coverage (Fig. 2b), while the gas pump processed sample (ethanol as the solvent) exhibits a somewhat mirror-like, compact, and pinhole-free surface morphology (Fig. 2c and S3†). For the heat treatment, the morphology of the PHABiI₄ film (ethanol as the solvent, see Fig. S5†) looks much better than that of the sample prepared using DMF as the solvent, which might be associated with the volatile nature of ethanol.

The process of perovskite growth from solution includes supersaturation, nucleation, and crystal growth. Two main factors for the fabrication of high-quality perovskite films are the density of nucleation sites and crystal growth time.³⁸ The

reason for the coarse morphology of the heat-treated sample is associated with the low nuclear density due to the low solvent evaporation rate of the heat treatment technique (Fig. 2b).¹⁸ Conversely, rapid solvent evaporation (within a few seconds) from solutions during gas pump treatment accelerates the supersaturation, resulting in a higher nuclear density, and then induces fast crystallization of uniformly sized Bi-based perovskite grains (see Fig. 2c).^{38,39} The above-mentioned relationship between the film morphology and nuclear density can be supported by the material nucleation/growth competition model in our previous work.⁴⁰ It is worth mentioning that the PHABiI₄ perovskite exhibits good solubility in ethanol, which is an eco-friendly and safe solvent.⁴¹ Furthermore, compared with the most widely used anti-solvent method,⁴² gas pump treatment technology is an environmentally benign processing route for the fabrication of high-quality lead-free perovskite films. For future research, it is apparent that more attention should be paid to solar cells or LEDs based on this Bi-based perovskite, just as the reports on lead-free halide double perovskites.^{43–45}

To study the effect of the chamber pressure on the film morphology, PHABiI₄ films were prepared by the gas pump treatment technique at different pressures. Dense and pinhole-free Bi-based perovskite films with a mirror-like surface (see Fig. S3†) were obtained when the pressure is from 1500 to 30 000 Pa. The process window is much larger than that of Pb-based⁴⁰ (100 to 1500 Pa) and Sn-based¹⁸ (20 to 1500 Pa) perovskite films reported in our previous work. The wide process window of this method might be beneficial for the large-scale manufacturing of lead-free perovskite films in the future. The grain size of the PHABiI₄ films is between 100 nm and 400 nm. As shown in Fig. S3,† the film samples prepared at different

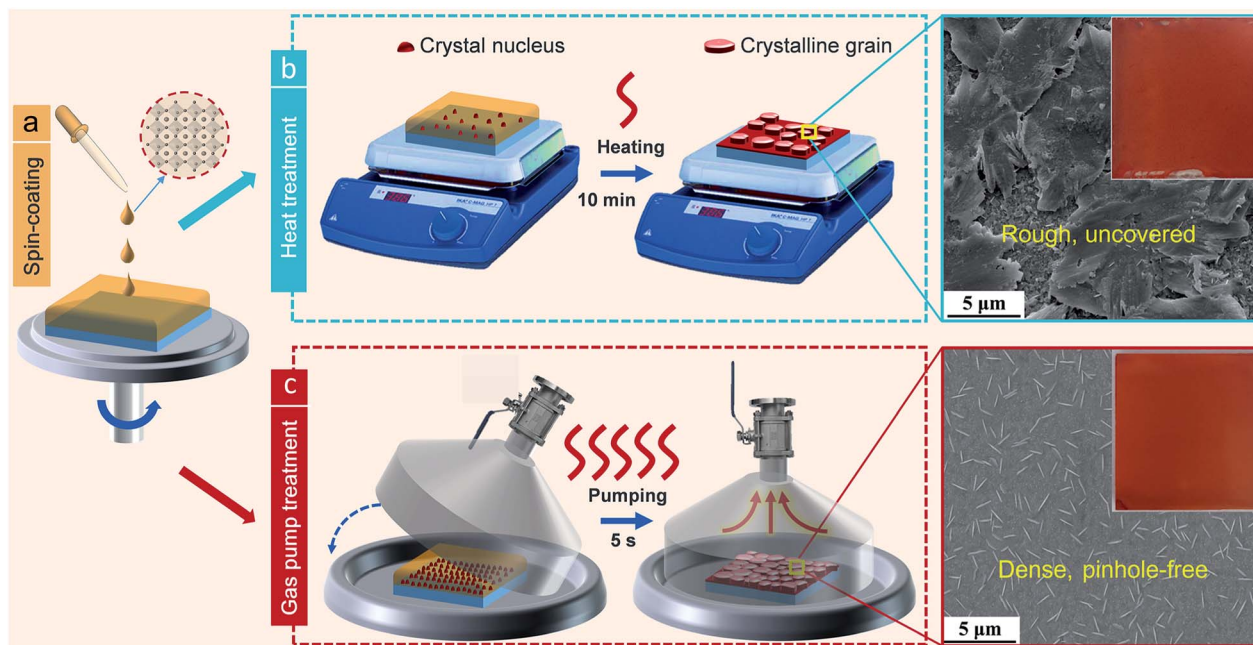


Fig. 2 (a) Bi-based perovskite solution was spin-coated onto a FTO substrate to form a perovskite liquid film. (b) Schematic mechanism, photograph, and SEM image of the (C₆H₅NH₃)BiI₄ film prepared by conventional heat treatment. (c) Schematic mechanism, photograph, and SEM image of the (C₆H₅NH₃)BiI₄ film prepared by gas pump treatment.

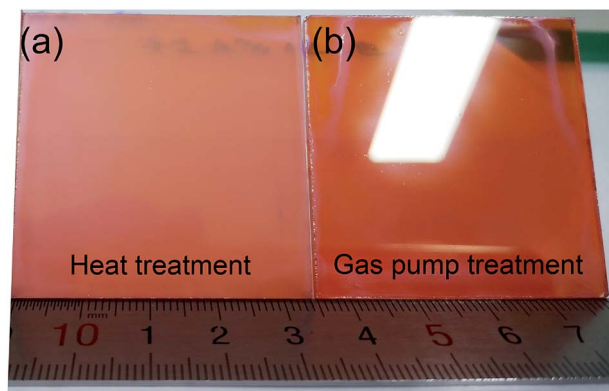


Fig. 3 Photographs of large-area (20.25 cm^2) Bi-based perovskite films fabricated by heat treatment (a) and gas pump treatment (b).

pressures exhibit almost the same morphology, suggesting the good consistency of the gas pump treatment. This phenomenon is consistent with our previously reported work.⁴⁰ The reason for this phenomenon may be attributed to the increase of grain size of the samples prepared at different pressures after heat treatment.⁴⁶ Besides, there are many rod-like crystals existing in PHABiI₄ films (see Fig. S3[†]). To explore this special phenomenon, we carried out EDS of rod-like crystals in the PHABiI₄ film (see Fig. S5[†]). The obtained Bi/I atomic ratio ($\approx 1 : 4$) of the rod-like crystals is consistent with the stoichiometry of the area without rod-like crystals, suggesting the compositional uniformity of the films. Furthermore, we compared the morphology of

the film samples with and without gas pump treatment. As shown in Fig. S4,[†] there are no rod-like crystals existing in the film without gas pump treatment. So, we speculate that the rod-like crystals in PHABiI₄ films might be associated with the extremely high solvent evaporation rate of the gas pump treatment.^{18,40} The detailed mechanism of the rod-like crystals is not clear now. Therefore, more attention should be paid to the detailed mechanism of the rod-like crystals in the future.

Large-area and high-quality film fabrication techniques are essential for the development of lead-free perovskite photovoltaic technology. Up to now, it is still challenging to fabricate large-area ($>20 \text{ cm}^2$) and high-quality Bi-based perovskite films by solution-based deposition methods. So, we try to fabricate large-area (20.25 cm^2) Bi-based perovskite films by conventional heat treatment and gas pump treatment. The PHABiI₄ film prepared by heat treatment shows a rough and dim surface (Fig. 3a), while the gas pump processed sample exhibits an obvious mirror-like surface (Fig. 3b). To the best of our knowledge, this is the first time that large-area and high-quality Bi-based perovskite thin films exceeding 20 cm^2 have been reported. The above-mentioned results suggest that gas-pump treatment is a powerful strategy for fabricating large-area and high-quality Bi-based perovskite thin films, which is vital for the scalable fabrication of Bi-based or other lead-free perovskite-based optoelectronic devices in the future.

To determine the absorption properties of the PHABiI₄ film, ultraviolet-visible (UV-vis) absorption and transmittance spectra were recorded (see Fig. 4a and S6[†]). The PHABiI₄ film shows strong distinct pre-edge absorption peaks at $\sim 2.7 \text{ eV}$, which

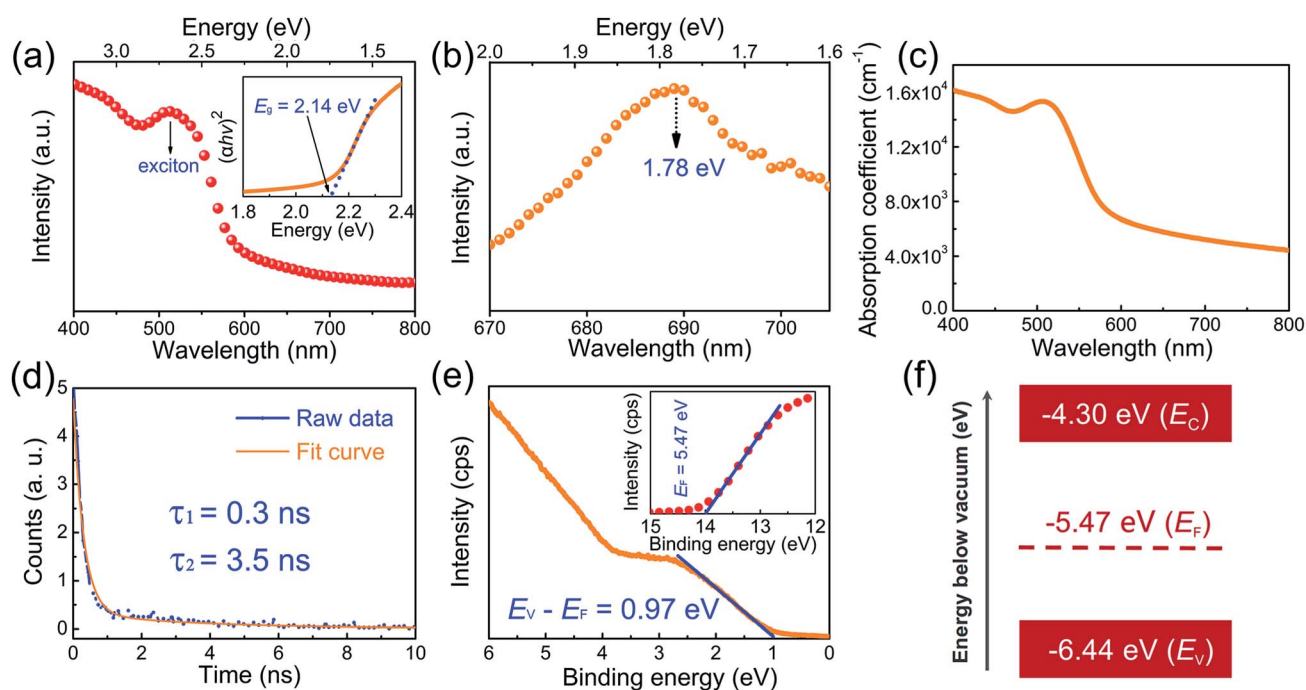


Fig. 4 (a) UV-vis spectrum of the $(\text{C}_6\text{H}_5\text{NH}_3)\text{BiI}_4$ film prepared by heat treatment. The inset is the Tauc plot of the $(\text{C}_6\text{H}_5\text{NH}_3)\text{BiI}_4$ film from the UV-vis spectrum to determine E_g under the assumption of a direct band gap. (b) Steady-state PL spectrum, (c) absorption coefficient, (d) time-resolved PL decay profile, and (e) UPS of the $(\text{C}_6\text{H}_5\text{NH}_3)\text{BiI}_4$ film prepared by heat treatment. The binding energy is calibrated with respect to He I photon energy (21.21 eV). (f) Band level diagram of the $(\text{C}_6\text{H}_5\text{NH}_3)\text{BiI}_4$ film calculated from the Tauc plot and UPS result.

might be related to the existence of excitons in this material (see Fig. 4a).³¹ From the corresponding Tauc plot of the PHABiI₄ thin film in the inset of Fig. 4a, a band gap (E_g) of 2.14 eV is obtained for PHABiI₄ assuming a direct E_g . If indirect E_g was instead assumed, an E_g of 2.03 eV would be obtained (Fig. S7†). Although this Bi-based perovskite is not suitable for single-junction photovoltaic devices, it might be used as a wide-bandgap absorber for multi-junction solar cells, as has been realized for CH₃NH₃PbBr₃ perovskites ($E_g = 2.26$ eV).⁴⁷ To further study the optical properties of the PHABiI₄ material, room-temperature photoluminescence (PL) was determined (Fig. 4b). Here we observe that the PL peak is shifted relative to the absorption onset, which is similar to previously reported results for Sb-based perovskites.³¹ The PL peak (*ca.* 1.78 eV) was shifted 360 meV to lower energies away from the band edge at 2.14 eV, suggesting radiative recombination involving sub-band-gap states.³¹ We also note that the full width at half

maximum of the PL spectrum was quite broad, which is similar to previously reported Bi-based perovskite materials.^{23,25} As shown in Fig. 4c, the absorption coefficient of the PHABiI₄ film is 1.54×10^4 cm⁻¹ for the most intense absorption at 510 nm, which is comparable to that of the MAPbI₃ perovskite.

To further study the exciton recombination dynamics, transient PL decay data were obtained using a time-correlated single-photon counting (TCSPC) setup. As shown in Fig. 4d, the raw data can be fitted well by a bi-exponential function, with a short lifetime of 0.3 ns (τ_1) and a long lifetime of 3.5 ns (τ_2), and the weight fractions are 58.04% (A_1) and 41.96% (A_2), respectively. The short lifetime might arise from the defect-induced nonradiative recombination, while the long lifetime might be attributed to the radiative recombination.⁴⁸ The average charge carrier lifetime (τ_{ave}) is calculated with the τ_i and A_i values from the fitted curve data (Fig. 4d) using the following equation:^{49,50}

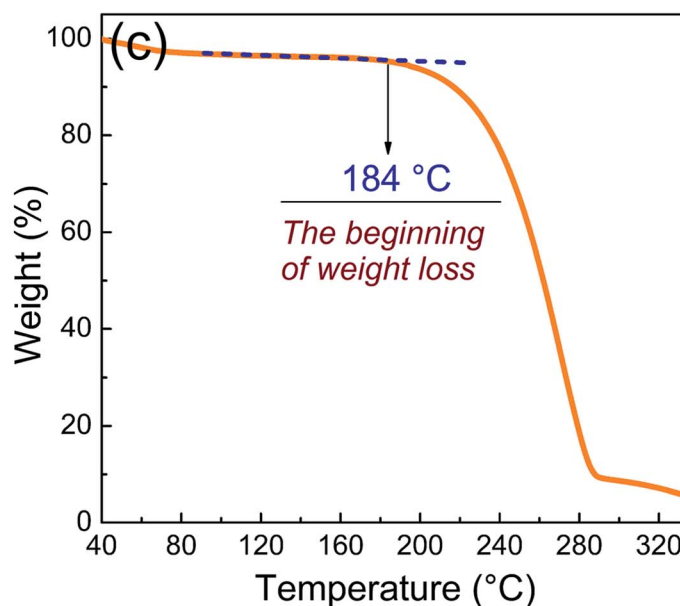
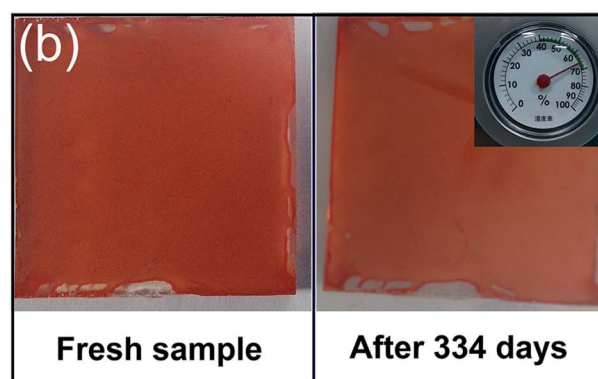
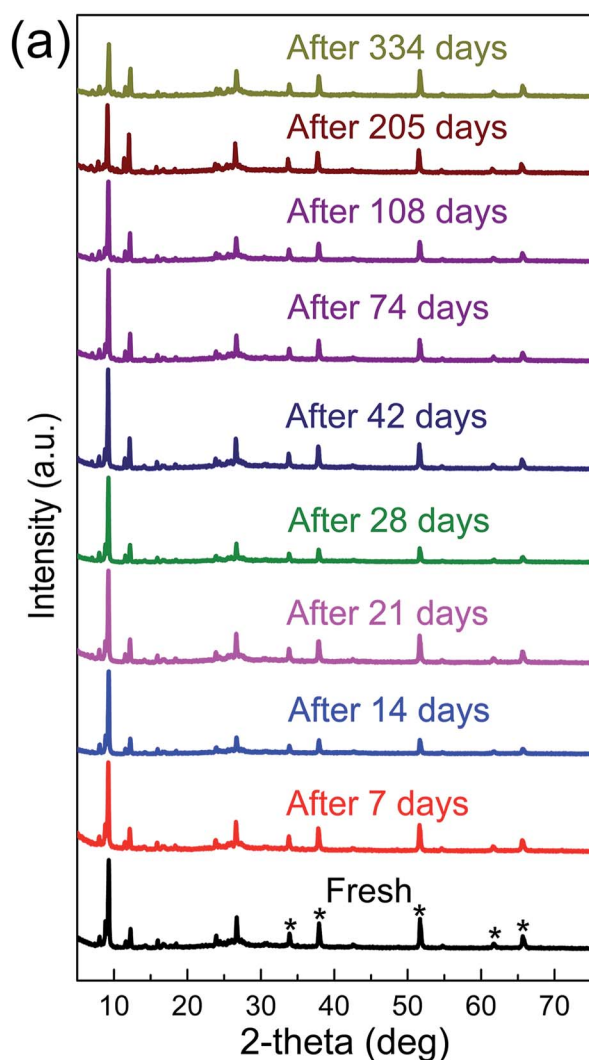


Fig. 5 (a) XRD patterns of the as-prepared (C₆H₅NH₃)BiI₄ film (prepared by heat treatment) and that after storage in ambient air (relative humidity of 50–70%) for 7, 14, 21, 28, 42, 74, 108, 205 and 334 days, measured from December 2017 to November 2018 in Xi'an, P. R. China. * indicates the peak of the FTO substrate. (b) Digital images of the as-prepared (C₆H₅NH₃)BiI₄ film (prepared by heat treatment) and that after storage in ambient air for 334 days. (c) TGA curve of (C₆H₅NH₃)BiI₄ materials.

$$\tau_{\text{avg}} = \sum_i A_i \tau_i, \quad \text{where} \quad \sum_i A_i = 1$$

The τ_{ave} ($1.64 \text{ ns} = 0.3 \text{ ns} \times 58.04\% + 3.5 \text{ ns} \times 41.96\%$) is longer than that of the Sn-based perovskite (MASnI_3 , 0.41 ns).⁵¹ During the early stages of research on this Bi-based material, the carrier lifetime (1.64 ns) was longer than the first-pass threshold value (1 ns) required for photovoltaic devices.²⁵ Thus, PHABiI_4 is worthy of being investigated as a promising photoelectric material in the future. Ultraviolet photoelectron spectroscopy (UPS) was performed to determine the Fermi energy (E_{F}) and valence band energy (E_{v}) level of the PHABiI_4 material. The E_{F} was estimated to be -5.47 eV , acquired using the cutoff energy (E_{cutoff}) presented in the inset of Fig. 4e from the equation $E_{\text{F}} = 21.22 \text{ eV (He I)} - E_{\text{cutoff}}$. The linear extrapolation in Fig. 4e represents the value of $E_{\text{v}} - E_{\text{F}}$, leading to an E_{v} of -6.44 eV . The conduction band energy (E_{c}) can be obtained by adding the E_{g} of the PHABiI_4 material to E_{v} , which is calculated to be -4.30 eV . The energy band diagram of the PHABiI_4 material is shown in Fig. 4f.

Inherent material stability toward moisture and heat is essential for the commercialization of perovskite-based optoelectronic devices. To study the moisture stability of the PHABiI_4 material, we exposed a PHABiI_4 sample continuously for 334 days to ambient air at 50–70% RH and recorded its XRD patterns (Fig. 5a and b). The sample for the moisture stability test was prepared by heat treatment, which is widely used in most lead-free perovskite materials ($\text{Cs}_3\text{Bi}_2\text{I}_9$, $\text{MA}_3\text{Bi}_2\text{I}_9$, AgBi_2I_7 , $\text{C}_6\text{H}_8\text{NBiI}_4$, $\text{C}_5\text{H}_6\text{NBiI}_4$, $\text{PMA}_2\text{CuBr}_4$, and $\text{Cs}_2\text{NaBiI}_6$, see Table S1†). As shown in Fig. S8,† a slight improvement of the peak intensity was observed after 42 days, suggesting the enhancement in crystallinity. This phenomenon might be associated with Ostwald ripening⁵² or age-induced recrystallization⁵³ reported in lead-based perovskite films. Besides, the color of the fresh film became slightly lighter after 334 days, which is consistent with the slight decrease of the peak intensity after 74, 108, 205 and 334 days. Despite this, the XRD patterns of the PHABiI_4 film do not show additional reflections over this long period of time. In contrast, the MAPbI_3 film is completely transformed into PbI_2 after approximately 40 days (52% RH).³⁵ Furthermore, the UV-vis spectra tests of the PHABiI_4 films were carried out before and after storage in ambient air for 14 and 28 days (Fig. S9†); no obvious changes were observed, suggesting that the PHABiI_4 material is humidity-stable. To compare with other lead-free halide perovskites, the ambient stability test results of lead-free halide perovskite materials reported in the literature are summarized (see Fig. 6 and Table S1†). To the best of our knowledge, this is the longest humidity stability reported to date for lead-free perovskite materials (see Fig. 6 and Table S1†). The remarkable long-term ambient stability of PHABiI_4 might be related to the hydrophobic PHA groups preventing the intrusion of water molecules in high humidity environments, as reported for two-dimensional (2D) perovskite materials.^{34–36} The detailed mechanisms of stability for this material might be complex and more studies are needed in the future. As shown in Fig. 5c, thermogravimetric analysis (TGA) results show the

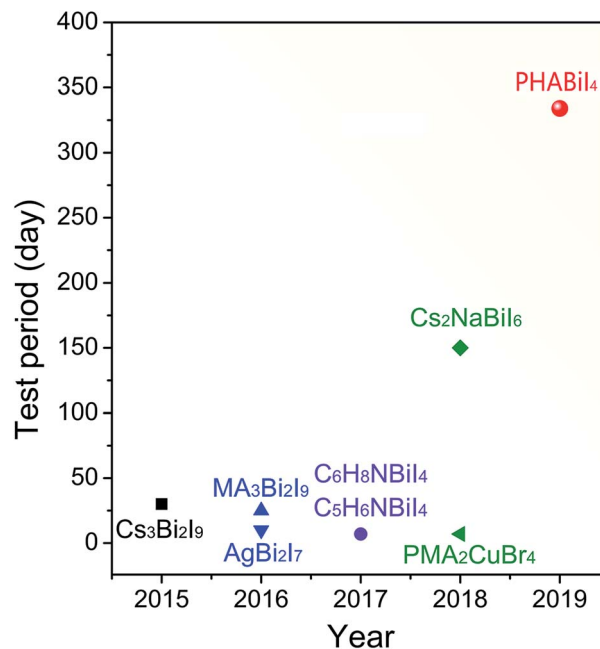


Fig. 6 Evolution of the test period of lead-free perovskite materials.

beginning of weight loss at $\sim 184^\circ \text{C}$, which means that PHABiI_4 -based solar cells could be used under actual working conditions, even though the device temperature exceeds 85°C .⁵⁴ These results clearly confirm the excellent moisture and heat stability of PHABiI_4 films.

To evaluate the photovoltaic performance of the PHABiI_4 perovskites, we fabricated solar cells with an architecture FTO/compact and mesoporous $\text{TiO}_2 + \text{PHABiI}_4/\text{P3HT}/\text{Au}$ (Fig. S10†). In our study, P3HT is used as the hole transport material (HTM) instead of the frequently used Spiro-OMeTAD, which was previously used for the $\text{PMA}_2\text{CuBr}_4$ (ref. 34) and AgBi_2I_7 (ref. 55) perovskite materials. The reason for using P3HT in the PHABiI_4 -based solar cell is that 4-*tert*-butylpyridine (used as an additive in the Spiro-OMeTAD solution) dissolves the PHABiI_4 layer.⁵⁶ Our initial attempts to incorporate PHABiI_4 into solar cells using this architecture obtained a moderate PCE of 0.78% (see Fig. S11†), which was comparable to the performance of other bismuth or antimony containing lead-free perovskite solar cells (see Table S2†). To exclude the contribution from the p-type P3HT polymer (a typical light-absorber in organic solar cells), we measured the J - V curve of the reference device without the PHABiI_4 layer, which showed a low PCE of 0.03% (Fig. S11†). The low PCE achieved during this early stage of investigation of this material might be associated with the following two reasons: first, the low V_{OC} (0.58 V) obtained for the device with PHABiI_4 is possibly due to the use of c- TiO_2 with disadvantageous energy levels, which may reduce the maximum voltage in the device. The E_{c} of PHABiI_4 (-4.30 eV) is higher than that of TiO_2 (-4.0 eV) (see Fig. S12†), which is not beneficial for photo-excited electron injection into n-type TiO_2 . Second, the fill factor (FF) of the device is very small (see Fig. S11†), which is similar to previously reported Bi-based solar cells.²³ The FF represents how “easy” or how “difficult” it is to extract the photo-excited

carriers out of a solar cell.⁵⁷ The relatively short carrier lifetime (1.64 ns, Fig. 4d) of this Bi-based material might not be beneficial for carrier transportation and collection⁵⁸ and will lower the FF.

Conclusions

In conclusion, we report the optoelectronic properties and stability of PHABiI₄ perovskite materials. We demonstrate that the gas pump treatment technique is an eco-friendly, robust approach for producing dense and pinhole-free Bi-based perovskite films. Remarkably, we successfully fabricated a large-area (>20 cm²) PHABiI₄ film, which is the largest Bi-based perovskite film ever reported. The PHABiI₄ perovskite exhibits good solubility in ethanol, an eco-friendly solvent. Most importantly, the PHABiI₄ material exhibits >330 days moisture stability, which is the longest humidity stability reported to date for lead-free perovskite materials. Our work provides a way to realize highly stable and lead-free perovskite materials for potential optoelectronic applications. Many future experimental and theoretical studies are needed to assess the full potential of this Bi-based perovskite material. We expect that this material may find its applications in LEDs, resistive switching memory, and photodetectors in the future.

Experimental section

Materials

All the chemicals were used as received, including BiI₃ (bismuth iodide, 99.99%, Aladdin), absolute ethanol (99.5%, Aladdin), chlorobenzene (anhydrous, 99.5%, Sigma-Aldrich), *N,N*-dimethylformamide (DMF, anhydrous, 99.8%, Sigma-Aldrich), poly(3-hexylthiophene) (P3HT, Xi'an Polymer Light Technology Corp), and C₆H₅NH₃I (phenylammonium iodide, >99.5%, Xi'an Polymer Light Technology Corp). Mesoporous TiO₂ (Dyesol, particle size ≈ 18 nm) paste was diluted with absolute ethanol (1 : 7 weight ratio). Fluorine-doped tin oxide (FTO)-coated glass (TEC7, 2.2 mm) was purchased from Ying Kou You Xuan Trade Co., Ltd (China). Stoichiometric C₆H₅NH₃I (221.04 mg) and BiI₃ (589.7 mg) were dissolved in 3 mL of absolute ethanol or DMF. Then, the dark red C₆H₅NH₃BiI₄ precursor solution (Fig. S13†) was stirred at 60 °C for 30 min.

Film fabrication

For the heat treatment, the precursor solution was dropped on the FTO substrates and spin coated at 2000 rpm for 30 s. For the gas pump treatment, the precursor solution was dropped on the FTO substrates and spin coated at 2000 rpm for 3 s. Subsequently, the sample was immediately transferred to a home-developed gas pump chamber³⁴ with different chamber pressures, pumping the sample for 5 s. All perovskite films were fabricated and annealed at 100 °C for 15 min.

Materials characterization

XRD measurements were carried out on an Ultima IV X-ray diffractometer with Cu K α from 5 to 80° (2 θ). The simulation

of the crystalline structure was performed on the Material Studio platform. UV-vis and transmission spectra were measured for the PHABiI₄ thin films spin-coated on the FTO substrate using a PerkinElmer Lambda 950 spectrophotometer. A transient fluorescence spectrometer (FLS980) was used for obtaining the transient PL decay curve and a 450 nm wavelength laser was used to excite the sample. Ultraviolet photoelectron spectroscopy (UPS) measurements were carried out with a Thermo Scientific ESCALAB 250Xi instrument, using monochromatic Al K α radiation ($h\nu = 1486.7$ eV). SEM tests were performed on a field-emission SEM (MIRA3 TESCAN). An SDT Q600 V20.5 Build 15 instrument was used for thermogravimetric analysis. The analysis was performed under a nitrogen atmosphere (flow rate 60 mL min⁻¹), and an interval from 42 to 450 °C (ramp rate of 10 °C min⁻¹) was studied. The samples for UV-vis and transmission spectroscopy, UPS, and long-term XRD tests were prepared by the most widely used heat treatment method.

Device fabrication and characterization

FTO substrates were cleaned by sonicating them sequentially in acetone, ethanol, and deionized water, each for 15 min, and then dried with nitrogen and treated in UV ozone for 30 min. A compact TiO₂ layer was prepared according to our previous report.^{18,40} The meso-TiO₂ solution was spin coated onto compact TiO₂ at 3000 rpm for 30 s, followed by annealing at 500 °C for 30 min. Then 0.3 M C₆H₅NH₃BiI₄ precursor in ethanol solution was dropped on the meso-TiO₂ layer and spin coated at 2000 rpm for 3 s. Subsequently, the sample was immediately transferred to a gas pump chamber with 3000 Pa, pumping the sample for 5 s. Then the somewhat mirror-like dried Bi-based perovskite films were heated at 100 °C for 15 min. Next, P3HT in chlorobenzene (20 mg mL⁻¹) was spin-coated at 4000 rpm for 30 s. Finally, a Au metal electrode was thermally evaporated. Photocurrent–voltage (*J*–*V*) curves of the devices with an active area of 0.1 cm² were recorded by using a source meter (2400, Keithley) under AM 1.5 G 100 mW cm⁻² illumination using a Peccell Technologies PEC-L01 solar simulator. The devices were tested by forward (from –0.2 to 1.2 V) voltage scanning with a sweep speed of 0.05 V s⁻¹.

Conflicts of interest

There are no conflicts to declare.

Acknowledgements

This work was financially supported by the National Program for Support of Top-notch Young Professionals. We thank Dr Chang Huang at the Instrument Analysis Center of Xi'an Jiaotong University for his assistance with long-term XRD tests.

References

- 1 S.-H. Turren-Cruz, A. Hagfeldt and M. Saliba, *Science*, 2018, **362**, 449–453.

- 2 M. He, B. Li, X. Cui, B. Jiang, Y. He, Y. Chen, D. O'Neil, P. Szymanski, M. A. El-Sayed, J. Huang and Z. Lin, *Nat. Commun.*, 2017, **8**, 16045.
- 3 X. Meng, X. Cui, M. Rager, S. Zhang, Z. Wang, J. Yu, Y. W. Harn, Z. Kang, B. K. Wagner, Y. Liu, C. Yu, J. Qiu and Z. Lin, *Nano Energy*, 2018, **52**, 123–133.
- 4 K. Lin, J. Xing, L. N. Quan, F. P. G. de Arquer, X. Gong, J. Lu, L. Xie, W. Zhao, D. Zhang, C. Yan, W. Li, X. Liu, Y. Lu, J. Kirman, E. H. Sargent, Q. Xiong and Z. Wei, *Nature*, 2018, **562**, 245–248.
- 5 Y. Cao, N. Wang, H. Tian, J. Guo, Y. Wei, H. Chen, Y. Miao, W. Zou, K. Pan, Y. He, H. Cao, Y. Ke, M. Xu, Y. Wang, M. Yang, K. Du, Z. Fu, D. Kong, D. Dai, Y. Jin, G. Li, H. Li, Q. Peng, J. Wang and W. Huang, *Nature*, 2018, **562**, 249–253.
- 6 H. Wei, D. DeSantis, W. Wei, Y. Deng, D. Guo, T. J. Savenije, L. Cao and J. Huang, *Nat. Mater.*, 2017, **16**, 826–833.
- 7 Q. Chen, J. Wu, X. Ou, B. Huang, J. Almutlaq, A. A. Zhumekenov, X. Guan, S. Han, L. Liang, Z. Yi, J. Li, X. Xie, Y. Wang, Y. Li, D. Fan, D. B. L. Teh, A. H. All, O. F. Mohammed, O. M. Bakr, T. Wu, M. Bettinelli, H. Yang, W. Huang and X. Liu, *Nature*, 2018, **561**, 88–93.
- 8 W.-Q. Liao, Y. Zhang, C.-L. Hu, J.-G. Mao, H.-Y. Ye, P.-F. Li, S. D. Huang and R.-G. Xiong, *Nat. Commun.*, 2015, **6**, 7338.
- 9 LNREL chart, <https://www.nrel.gov/pv/assets/images/efficiency-chart.png>, accessed Oct 10, 2018.
- 10 A. Babayigit, A. Ethirajan, M. Muller and B. Conings, *Nat. Mater.*, 2016, **15**, 247–251.
- 11 J. Bisquert, Y. Qi, T. Ma and Y. Yan, *ACS Energy Lett.*, 2017, **2**, 520–523.
- 12 A. C. Williams and B. W. Barry, *Adv. Drug Delivery Rev.*, 2012, **64**, 128–137.
- 13 J. Zhao, L. Wei, C. Jia, H. Tang, X. Su, Y. Ou, Z. Liu, C. Wang, X. Zhao, H. Jin, P. Wang, G. Yu, G. Zhang and J. Liu, *J. Mater. Chem. A*, 2018, **6**, 20224–20232.
- 14 S. Yang, W. Fu, Z. Zhang, H. Chen and C.-Z. Li, *J. Mater. Chem. A*, 2017, **5**, 11462–11482.
- 15 Z. Xiao, W. Meng, J. Wang, D. B. Mitzi and Y. Yan, *Mater. Horiz.*, 2017, **4**, 206–216.
- 16 S. Tsarev, A. G. Boldyreva, S. Y. Luchkin, M. Elshobaki, M. I. Afanasov, K. J. Stevenson and P. A. Troshin, *J. Mater. Chem. A*, 2018, **6**, 21389–21395.
- 17 W. Ke and M. G. Kanatzidis, *Nat. Commun.*, 2019, **10**, 965.
- 18 X. Li, L. Gao, Q. Chu, Y. Li, B. Ding and G. Yang, *ACS Appl. Mater. Interfaces*, 2019, **11**, 3053–3060.
- 19 C. Ran, J. Xi, W. Gao, F. Yuan, T. Lei, B. Jiao, X. Hou and Z. Wu, *ACS Energy Lett.*, 2018, **3**, 713–721.
- 20 M. Chen, M. G. Ju, H. F. Garces, A. D. Carl, L. K. Ono, Z. Hawash, Y. Zhang, T. Shen, Y. Qi, R. L. Grimm, D. Pacifici, X. C. Zeng, Y. Zhou and N. P. Padture, *Nat. Commun.*, 2019, **10**, 16.
- 21 P. Cheng, T. Wu, J. Zhang, Y. Li, J. Liu, L. Jiang, X. Mao, R. F. Lu, W. Q. Deng and K. L. Han, *J. Phys. Chem. Lett.*, 2017, **8**, 4402–4406.
- 22 T. Krishnamoorthy, H. Ding, C. Yan, W. L. Leong, T. Baikie, Z. Zhang, M. Sherburne, S. Li, M. Asta, N. Mathews and S. G. Mhaisalkar, *J. Mater. Chem. A*, 2015, **3**, 23829–23832.
- 23 B. W. Park, B. Philippe, X. Zhang, H. Rensmo, G. Boschloo and E. M. Johansson, *Adv. Mater.*, 2015, **27**, 6806–6813.
- 24 Z. Zhang, X. Li, X. Xia, Z. Wang, Z. Huang, B. Lei and Y. Gao, *J. Phys. Chem. Lett.*, 2017, **8**, 4300–4307.
- 25 R. L. Hoyer, R. E. Brandt, A. Osherov, V. Stevanovic, S. D. Stranks, M. W. Wilson, H. Kim, A. J. Akey, J. D. Perkins, R. C. Kurchin, J. R. Poindexter, E. N. Wang, M. G. Bawendi, V. Bulovic and T. Buonassisi, *Chem.–Eur. J.*, 2016, **22**, 2605–2610.
- 26 C. Ran, Z. Wu, J. Xi, F. Yuan, H. Dong, T. Lei, X. He and X. Hou, *J. Phys. Chem. Lett.*, 2017, **8**, 394–400.
- 27 T. Li, Y. Hu, C. A. Morrison, W. Wu, H. Han and N. Robertson, *Sustainable Energy Fuels*, 2017, **1**, 308–316.
- 28 S. M. Jain, D. Phuyal, M. L. Davies, M. Li, B. Philippe, C. De Castro, Z. Qiu, J. Kim, T. Watson, W. C. Tsoi, O. Karis, H. Rensmo, G. Boschloo, T. Edvinsson and J. R. Durrant, *Nano Energy*, 2018, **49**, 614–624.
- 29 C. Cuhadar, S. G. Kim, J. M. Yang, J. Y. Seo, D. Lee and N. G. Park, *ACS Appl. Mater. Interfaces*, 2018, **10**, 29741–29749.
- 30 M. Leng, Y. Yang, Z. Chen, W. Gao, J. Zhang, G. Niu, D. Li, H. Song, J. Zhang, S. Jin and J. Tang, *Nano Lett.*, 2018, **18**, 6076–6083.
- 31 J.-C. Hebig, I. Kühn, J. Flohre and T. Kirchartz, *ACS Energy Lett.*, 2016, **1**, 309–314.
- 32 X. Li, X. Zhong, Y. Hu, B. Li, Y. Sheng, Y. Zhang, C. Weng, M. Feng, H. Han and J. Wang, *J. Phys. Chem. Lett.*, 2017, **8**, 1804–1809.
- 33 Y. Liu, X. Li, J. Wang, L. Xu and B. Hu, *J. Mater. Chem. A*, 2017, **5**, 13834–13841.
- 34 X. Li, B. Li, J. Chang, B. Ding, S. Zheng, Y. Wu, J. Yang, G. Yang, X. Zhong and J. Wang, *ACS Appl. Energy Mater.*, 2018, **1**, 2709–2716.
- 35 I. C. Smith, E. T. Hoke, D. Solis-Ibarra, M. D. McGehee and H. I. Karunadasa, *Angew. Chem., Int. Ed.*, 2014, **53**, 11232–11235.
- 36 H. Tsai, W. Nie, J.-C. Blancon, C. C. Stoumpos, R. Asadpour, B. Harutyunyan, A. J. Neukirch, R. Verduzco, J. J. Crochet, S. Tretiak, L. Pedesseau, J. Even, M. A. Alam, G. Gupta, J. Lou, P. M. Ajayan, M. J. Bedzyk, M. G. Kanatzidis and A. D. Mohite, *Nature*, 2016, **536**, 312–316.
- 37 J. Shin, M. Kim, S. Jung, C. S. Kim, J. Park, A. Song, K.-B. Chung, S.-H. Jin, J. H. Lee and M. Song, *Nano Res.*, 2018, **11**, 6283–6293.
- 38 K.-F. Lin, S. H. Chang, K.-H. Wang, H.-M. Cheng, K. Y. Chiu, K.-M. Lee, S.-H. Chen and C.-G. Wu, *Sol. Energy Mater. Sol. Cells*, 2015, **141**, 309–314.
- 39 Y. Li, X. L. He, B. Ding, L. L. Gao, G. J. Yang, C. X. Li and C. J. Li, *J. Power Sources*, 2016, **320**, 204–211.
- 40 B. Ding, Y. Li, S. Y. Huang, Q. Q. Chu, C. X. Li, C. J. Li and G. J. Yang, *J. Mater. Chem. A*, 2017, **5**, 6840–6848.
- 41 H. Li, C. Wu, Y. Yan, B. Chi, J. Pu, J. Li and S. Priya, *ChemSusChem*, 2017, **10**, 3994–3998.
- 42 N. J. Jeon, J. H. Noh, Y. C. Kim, W. S. Yang, S. Ryu and S. I. Seok, *Nat. Mater.*, 2014, **13**, 897–903.

- 43 M. Pantaler, K. T. Cho, V. Queloz, I. Garcia Benito, C. Fettkenhauer, I. Anusca, M. K. Nazeeruddin, D. C. Lupascu and G. Grancini, *ACS Energy Lett.*, 2018, **3**, 1781–1786.
- 44 M. Chen, M. G. Ju, A. D. Carl, Y. X. Zong, R. L. Grimm, J. J. Gu, X. C. Zeng, Y. Y. Zhou and N. P. Padture, *Joule*, 2018, **2**, 558–570.
- 45 J. Luo, X. Wang, S. Li, J. Liu, Y. Guo, G. Niu, L. Yao, Y. Fu, L. Gao, Q. Dong, C. Zhao, M. Leng, F. Ma, W. Liang, L. Wang, S. Jin, J. Han, L. Zhang, J. Etheridge, J. Wang, Y. Yan, E. H. Sargent and J. Tang, *Nature*, 2018, **563**, 541–545.
- 46 X. Wang, S. Kustov, B. Verlinden and J. Van Humbeeck, *Shape Memory and Superelasticity*, 2015, vol. 1, pp. 231–239.
- 47 R. Sheng, A. W. Ho-Baillie, S. Huang, M. Keevers, X. Hao, L. Jiang, Y. B. Cheng and M. A. Green, *J. Phys. Chem. Lett.*, 2015, **6**, 3931–3934.
- 48 B. Yang, J. S. Chen, F. Hong, X. Mao, K. B. Zheng, S. Q. Yang, Y. J. Li, T. Pullerits, W. Q. Deng and K. L. Han, Lead-Free, Air-Stable All-Inorganic Cesium Bismuth Halide Perovskite Nanocrystals, *Angew. Chem., Int. Ed.*, 2017, **56**, 12471–12475.
- 49 J. H. Heo, H. J. Han, D. Kim, T. K. Ahn and S. H. Im, *Energy Environ. Sci.*, 2015, **8**, 1602–1608.
- 50 M. Duan, Y. Rong, A. Mei, Y. Hu, Y. Sheng, Y. Guan and H. Han, *Carbon*, 2017, **120**, 71–76.
- 51 W. Ke, C. C. Stoumpos, I. Spanopoulos, L. Mao, M. Chen, M. R. Wasielewski and M. G. Kanatzidis, *J. Am. Chem. Soc.*, 2017, **139**, 14800–14806.
- 52 M. Yang, T. Zhang, P. Schulz, Z. Li, G. Li, D. H. Kim, N. Guo, J. J. Berry, K. Zhu and Y. Zhao, *Nat. Commun.*, 2016, **7**, 12305.
- 53 C. Fei and H. Wang, *Org. Electron.*, 2019, **68**, 143–150.
- 54 B. Conings, J. Drijkoningen, N. Gauquelin, A. Babayigit, J. D'Haen, L. D'Olieslaeger, A. Ethirajan, J. Verbeeck, J. Manca, E. Mosconi, F. D. Angelis and H.-G. Boyen, *Adv. Energy Mater.*, 2015, **5**, 1500477.
- 55 Y. Kim, Z. Yang, A. Jain, O. Voznyy, G. H. Kim, M. Liu, L. N. Quan, F. P. Garcia de Arquer, R. Comin, J. Z. Fan and E. H. Sargent, *Angew. Chem., Int. Ed.*, 2016, **55**, 9586–9590.
- 56 M. B. Johansson, H. Zhu and E. M. Johansson, *J. Phys. Chem. Lett.*, 2016, **7**, 3467–3471.
- 57 B. Qi and J. Wang, *Phys. Chem. Chem. Phys.*, 2013, **15**, 8972–8982.
- 58 D. W. de Quilettes, S. M. Vorpahl, S. D. Stranks, H. Nagaoka, G. E. Eperon, M. E. Ziffer, H. J. Snaith and D. S. Ginger, *Science*, 2015, **348**, 683–686.